農業工程學報 第40卷 第3期
中華民國83年9月出版

Journal of Chinese Agricultural Engineering
Vol. 40, No. 3, September 1994

泥砂滲入孔隙介質之序率模式研究(二)
實驗結果與應用部份

Stochastic Modeling of Sediment Infiltration into Porous Media
Phase II: Experimental Results and Application

國立臺灣大學水工試驗所 副研究員

吳 富 春

Fu-Chun Wu

摘 要

由於泥砂滲入孔隙介質之過程是一種非恆定、非均勻之過程，一名爲非均質波益桑程序模式之序率模式適合用以描述具這種特性之過程。然而在應用這種序率模式時，須確知兩個參函數λ_1和λ_2。λ_1和λ_2之物理意義分別爲平均停息時間之倒數和平均步長之倒數如果將泥砂顆粒之移動考慮成一系列之交替步移與停息。本研究之第一部份乃推演決定兩個參函數λ_1和λ_2之理論。根據這理論，本研究之第二部份乃以實驗方法決定λ_1和λ_2，並將所得之結果加以討論及分析以供進一步之應用。

關鍵詞：序率模式，泥砂入滲，孔隙介質

ABSTRACT

A stochastic model, non-homogeneous Poisson process model, is adopted to describe the physical process of sediment particles infiltration into the porous media because of this model's suitability for the unsteady and non-uniform nature of the sediment infiltration process as well as the random behavior of the sediment particles within the porous matrix. Two parameters of this model, λ_1 and λ_2, are needed for stochastic modeling of this process. Physically, λ_1 and λ_2 are two intensity functions representing the inverse of the average rest period and the inverse of the average step length if the movement of the sediment particles is considered as a series of alternate step and rest. In phase I of this study, the theoretical bases for determination of λ_1 and λ_2 are presented. In phase II, an experimental study based on the theories from phase I is conducted to evaluate λ_1 and λ_2. The experimental results are discussed and analyzed for further application.

Key words: Stochastic Model, Sediment Infiltration, Porous Media

INTRODUCTION

The stochastic modeling of the physical process of sediment particles infiltration into the porous media was discussed in phase I of this study (Wu, 1994), and the theoretical bases for determination of the intensity functions of the non-homogeneous Poisson process (NHPP) model, λ_1 and λ_2, were also presented. In order to evaluate the two parameters λ_1 and λ_2, a series of sediment infiltration experiments were performed to physically measure the time and spatial variations of sediment distribution within the void space of the porous matrix. In this paper of phase II study, the experiments are described and the results are analyzed and generalized to functional forms in terms of the medium-sediment size ratio, the total amount of sediment input, and the seepage flow rate by regression for further application.

EXPERIMENTAL STUDY

The experiments of sediment infiltration into the gravel column were conducted in the Hydraulic Engineering Laboratory, University of California at Berkeley, in order to determine the intensity functions λ_1 and λ_2, as well as to ascertain the behavior of such intensity functions.

Experimental Setup

The experimental apparatus consists of the parts as shown in Fig. 1. They are: A) gravel column, B) flow meter, C) valve controlling outflow, D) outflow pipe line, E) sedimentation basin, F) recirculating tank, G) electronic pump, H) valve controlling inflow, I) inflow pipe line, J) sand container. The square column is made of transparent Lucite plates, 58 cm in height and the internal dimension is 25 cm × 25 cm. This plastic column consists of six 5-cm-thick layers in the middle part, which can be taken apart layer by layer for collecting the gravel-sand samples after each experimental run. The seepage flow controlling devices include a flow meter below the outlet of the plastic column and two valves at the inflow line and outflow line respectively. By adjusting the two valves, the seepage flow can reach a steady flow rate indicated on the flow meter. The outflow treatment system includes a sedimentation basin and two recirculating tanks. The sands penetrating through the gravel column are carried by the flow toward the sedimentation basin where the sands settle down at the bottom of the basin, and the treated water is directed into the recirculating tanks through the connecting pipe. The treated water is then pumped up to the gravel column system through the inflow pipe line.

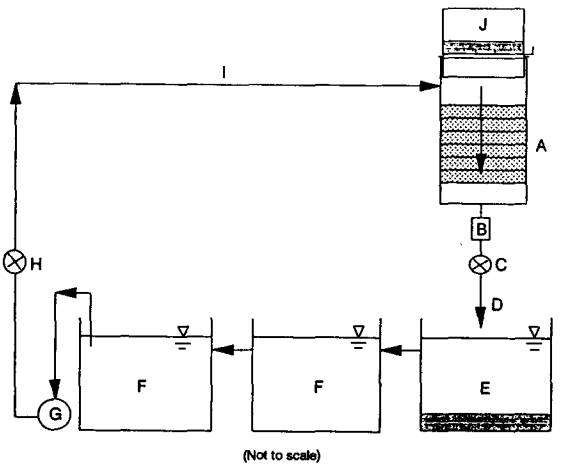

Figure 1. Schematic diagram of the experimental setup

Materials

Two kinds of well-sorted gravel, type A and type B, were used as the porous media in the plastic column. Three kinds of sand, #1C, #30 and #60, were used as the fine particles infiltrating into the porous matrix. The essential properties of these materials are summarized in Table 1, where the fall velocity, ω, is calculated by Rubey's formula based on d_{50} (Garde and Ranga Raju, 1985). The liquid used in the experiments was the water from the municipal

utility supply system. The water temperature ranged from 13°C to 18°C with an average of 16° C.

TABLE 1. Essential Properties of the Experiment Materials

Gravel			Sand			
	D_{15} (mm)	D_{50} (mm)		d_{50} (mm)	d_{85} (mm)	Fall velocity, ω (cm/sec)
Type A	6.7	7.5	#1C	0.87	1.10	8.96
Type B	5.1	5.8	#30	0.42	0.55	5.30
			#60	0.34	0.41	4.32

Experimental Procedures

The general procedures for each experimental run were as follows:

1. The detached layers of the plastic column were assembled and then packed with a 30-cm-thick clean gravel matrix.
2. The pump was turned on and the two valves were adjusted until the flow reached the steady state with a desired seepage flow rate.
3. A sand container, loaded with the predetermined amount of sand (M_T), was placed on top of the plastic column and was opened instantaneously at time t_0 by pulling out the steel plate such that all of the sands fell onto the gravel bed surface simultaneously, as the gravel bed configuration at time t_0 shown in Fig. 2. The plate was pulled out as quickly as possible to minimize the effects of non-uniformity in time and space.
4. The infiltration of sand particles into the gravel matrix was observed through the transparent wall of the plastic column.
5. The pump was turned off at time t and the water in the gravel column system as well as the pipe lines was all drained out.
6. The plastic column was taken apart layer by layer to collect: a) the sands left on top of the gravel bed surface, and b) the gravel-sand mixture samples from the six 5-cm-thick layers.
7. The sand and gravel-sand samples were dried in the oven. After being cooled down, the sands in the dried gravel-sand samples were sieved out.
8. The amount of sand left on top of the gravel bed surface (m_0), and the amount of sand deposition within the top 5-cm-thick layer of the gravel matrix (m_1) through the amount of sand deposition within the bottom 5-cm-thick layer of the gravel matrix (m_6), as the gravel bed configuration at time t illustrated in Fig. 2, were measured by weight.

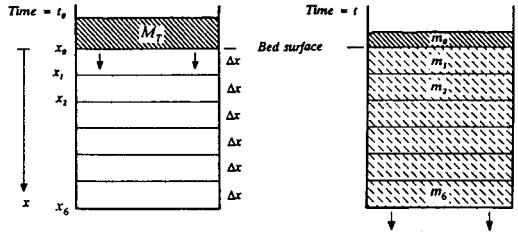

Figure 2. Gravel matrix configurations at time t_0 and time t

Testing Conditions

According to the conclusions drawn from the granular filter experiments by Yim and Sternberg (1987) as well as the observations from the present investigation, there are four experimental variables that are considered as the primary factors influencing the experimental performance. In all, a total of 41 runs with different testing conditions were performed. These included two types of gravel (type A and type B); three kinds of sand (#1C, #30 and #60); total amount of sand input in the range between 1 kg (2.2 lb) and 16 kg (35.2 lb); seepage flow rate ranging from 63.08×10^{-6} m^3/sec (1 gpm) to 37.85×10^{-5} m^3/sec (6 gpm). A summary of these testing conditions is given in Table 2, in which the gravel-sand size ratio, R_s, is defined as D_{15}/d_{85} according to Sherard et al. (1984). Among these experiments, there were 11 such runs that the clogging state (or stable state) of the sand particles at the top layer of the gravel column was reached. As was mentioned in the previous paper (Wu, 1994), once the clogging state near the bed surface was reached, further sediment infiltration was restricted and thus all the sand particles within the gravel matrix stayed stably at their places.

TABLE 2. Summary of testing conditions for the 41 experimental runs

Exp. No.	Gravel Type	Sand Type	Size Ratio, R_s D_{15}/d_{85}	Total Sand Input kg	(lb.)	Seepage Flow Rate $\times 10^{-6} m^3/sec$	(gpm)	Running Time (sec)
1*	A	#1C	6.1	2	(4.4)	126.16	(2)	120
2	A	#30	12.1	1	(2.2)	63.08	(1)	5
3	A	#30	12.1	1	(2.2)	63.08	(1)	20
4*	A	#30	12.1	1	(2.2)	63.08	(1)	180
5	A	#30	12.1	2	(4.4)	63.08	(1)	10
6	A	#30	12.1	2	(4.4)	63.08	(1)	30
7*	A	#30	12.1	2	(4.4)	63.08	(1)	90
8	A	#30	12.1	2	(4.4)	126.16	(2)	60
9	A	#30	12.1	2	(4.4)	126.16	(2)	600
10	A	#30	12.1	2	(4.4)	126.16	(2)	1200
11*	A	#30	12.1	2	(4.4)	126.16	(2)	2400
12	A	#30	12.1	2	(4.4)	189.24	(3)	10
13	A	#30	12.1	2	(4.4)	189.24	(3)	30
14	A	#30	12.1	2	(4.4)	189.24	(3)	60
15*	A	#30	12.1	2	(4.4)	189.24	(3)	360
16	A	#30	12.1	2	(4.4)	252.32	(4)	60
17	A	#30	12.1	2	(4.4)	378.48	(6)	60
18*	A	#30	12.1	3	(6.6)	63.08	(1)	300
19	A	#30	12.1	3	(6.6)	378.48	(6)	60
20	A	#30	12.1	4	(8.8)	126.16	(2)	60
21	A	#30	12.1	4	(8.8)	378.48	(6)	60
22	A	#30	12.1	4	(8.8)	378.48	(6)	600
23*	A	#30	12.1	4	(8.8)	378.48	(6)	1800
24	A	#60	16.3	2	(4.4)	63.08	(1)	240
25	A	#60	16.3	2	(4.4)	126.16	(2)	30
26	A	#60	16.3	2	(4.4)	126.16	(2)	300
27	A	#60	16.3	2	(4.4)	126.16	(2)	1200
28	A	#60	16.3	2	(4.4)	126.16	(2)	3600
29	A	#60	16.3	4	(8.8)	126.16	(2)	1200
30	A	#60	16.3	8	(17.6)	126.16	(2)	1200
31	A	#60	16.3	16	(35.3)	126.16	(2)	1200
32	B	#30	9.3	2	(4.4)	63.08	(1)	5
33	B	#30	9.3	2	(4.4)	63.08	(1)	15
34	B	#30	9.3	2	(4.4)	63.08	(1)	30
35*	B	#30	9.3	2	(4.4)	63.08	(1)	120
36*	B	#60	12.6	1	(2.2)	63.08	(1)	540
37	B	#60	12.6	2	(4.4)	63.08	(1)	5
38*	B	#60	12.6	2	(4.4)	63.08	(1)	540
39	B	#60	12.6	2	(4.4)	126.16	(2)	1080
40*	B	#60	12.6	4	(8.8)	63.08	(1)	540
41	B	#60	12.6	8	(17.6)	63.08	(1)	540

* The stable state (clogging at the top layer) was reached.

RESULTS AND ANALYSIS

Experimental Results

For each experimental run, the amount of sand stayed on top of the gravel bed surface (m_0) and the sand deposits within the six 5-cm-thick layers (m_1, m_2, m_3, m_4, m_5, m_6) were measured as described in the previous section. Table 3 lists all the results of the 41 experiments.

Analysis

1. Cumulative probability distribution, $F_t(x)$

According to the preceding paper of this study (Wu, 1994), the cumulative probability distribution at time t_i , $F_{t_i}(x)$, is given as

$$F_{t_i}(x) = P(X_{t_i} \le x) = \frac{m_x(t_i)}{M_T} \qquad (1)$$

where $m_x(t_i)$ is the amount of sediment that can be found above the depth x of the porous matrix at time t_i , M_T is the total amount of sediment initially at the bed surface, as shown in Fig. 2. The values of $F_{t_i}(x)$ were calculated from the sand deposits at seven locations along the depth of the gravel matrix at time t_i which were physically measured in the present study.

Figs. 3 and 4 are typical cumulative probability distribution curves along the depth from the gravel matrix surface for various running times under A30-2-F3 condition (i.e. type A gravel, 2 kg of #30 sand, and seepage flow rate at 3 gpm) and A60-2-F2 condition. It is noticed that the amount of sand on the gravel bed surface (i.e. at x = 0cm) kept decreasing whereas the amount of sand passing through the bottom of the gravel matrix (i.e. at x = 30cm) kept increasing until the infiltration process reached the so-called stable state, which is the state that clogging of the sands occurs at the top layer of the gravel matrix. The clogging of the sands prevents more sand particles from infiltrating into the deeper layers. As observed in the laboratory, there is hardly any sand particle penetrating through the bottom of the filter at this stage except that occasionally two or three sand particles fall down from the bottom of the gravel matrix. The curve of 360 seconds in Fig. 3 is the stable-state curve for the reason that the experiments resulted in almost identical cumulative distribution curves after 360 seconds. It is also noticed that generally the sand deposit in each layer was increasing before the stable state was reached, except for those situations the sands were too fine to be trapped within the porous matrix (e.g. A60-2-F2 series in Fig. 4).

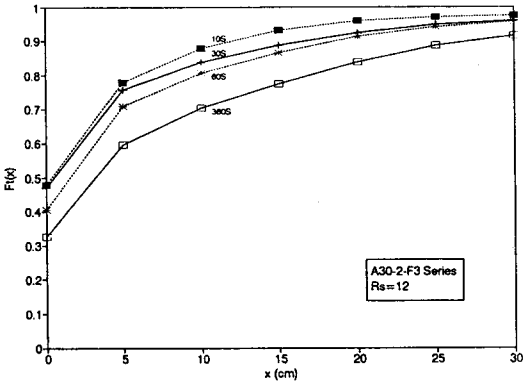

Figure 3. $F_t(x)$ curves of A30-2-F3 series experiments

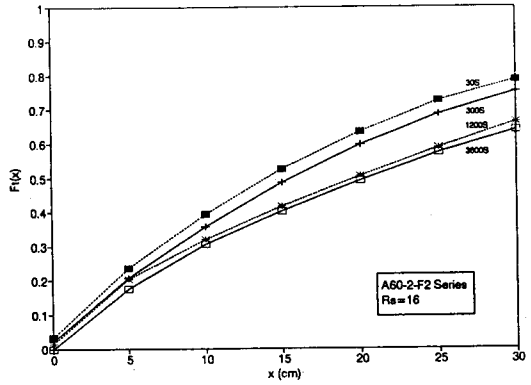

Figure 4. $F_t(x)$ curves of A60-2-F2 series experiments

Variation of $F_t(x)$ with the Size Ratio, R_s

The shape and magnitude of the $F_t(x)$ curve are very much dependent on the size ratio R_s. Some $F_t(x)$ curves for various size ratios at the stable state, under the specified total input and seepage flow conditions, are shown in Fig. 5. Evidently they are correlated to the size ratio, R_s. From Fig. 5, it is seen that for low R_s, the sands

TABLE 3. Summary of experimental results (unit: gram)

Exp. No.	m_0	m_1	m_2	m_3	m_4	m_5	m_6
1	1638.25	298.49	24.36	2.76	0.91	0.49	0.48
2	305.43	501.38	114.03	38.88	14.79	4.21	1.78
3	252.09	517.13	128.61	46.39	17.38	8.20	2.55
4	252.00	514.90	126.63	43.03	17.77	8.17	2.55
5	954.28	639.63	200.96	79.95	45.91	21.33	8.69
6	940.56	641.63	199.77	79.41	40.20	28.00	14.92
7	931.64	602.1	198.51	100.68	57.89	30.07	11.32
8	1047.83	486.51	195.07	93.90	62.46	32.58	18.33
9	755.02	545.92	233.00	123.40	95.08	73.34	45.02
10	727.46	488.31	261.20	162.25	106.61	77.20	47.00
11	642.48	584.62	242.76	144.42	120.04	98.76	49.62
12	957.35	601.66	198.69	102.75	58.12	21.79	8.55
13	939.85	573.77	163.71	98.29	71.83	46.84	26.17
14	811.74	606.52	195.86	119.32	92.89	57.10	29.54
15	652.47	541.06	212.98	142.64	127.92	97.59	55.31
16	695.09	492.03	251.92	160.56	119.42	87.34	50.71
17	567.74	509.85	253.04	168.86	135.33	99.11	51.88
18	1895.78	676.72	177.03	90.01	49.97	29.80	14.64
19	1233.10	538.00	268.69	192.40	186.04	141.53	99.16
20	2550.96	552.98	306.01	188.31	123.24	73.47	35.87
21	2005.98	566.24	282.98	222.47	210.90	149.18	103.51
22	1305.07	595.34	374.28	271.60	260.36	237.45	177.13
23	391.09	425.40	332.05	268.03	284.42	288.14	218.88
24	77.10	425.86	254.22	195.96	195.65	159.47	129.51
25	65.66	407.20	313.15	264.53	217.88	181.52	118.78
26	41.22	374.15	298.62	258.31	221.53	177.42	129.58
27	27.50	381.82	229.26	194.18	174.61	167.10	146.46
28	0.00	349.31	263.21	192.74	176.06	163.79	128.48
29	171.89	420.00	242.55	274.68	248.17	230.10	209.00
30	336.35	605.56	411.33	324.51	283.29	371.12	393.21
31	878.24	789.47	686.04	695.29	549.67	472.90	395.38
32	1628.37	314.67	22.34	3.61	1.39	0.99	0.76
33	1620.56	327.55	21.52	3.18	1.14	0.77	0.73
34	1594.53	338.90	20.64	2.62	0.92	0.66	0.58
35	1465.21	443.08	49.46	7.06	2.49	1.13	0.80
36	204.29	459.98	156.86	86.77	43.77	20.33	6.67
37	1112.11	516.42	153.95	90.44	41.49	25.88	9.63
38	998.68	549.43	177.24	107.30	60.21	34.23	13.72
39	506.93	462.32	284.90	193.30	173.85	124.73	61.51
40	2806.54	576.30	182.45	112.03	95.90	60.00	33.94
41	6023.64	576.45	266.59	208.62	217.62	178.87	81.21

are deposited mostly in the top one or two layers but rarely in the middle and bottom layers. However, the sand deposition is much more uniformly distributed in each layer for high R_s. For example in Fig. 5: 1) for the curve with $R_s = 6$, nearly all the sands are deposited in the first layer (from 0 to 5 cm) and over 80% of the sands stay on the gravel matrix surface; 2) for the curve with $R_s = 16$, the $F_t(x)$ curve is close to a straight line, which means that the sand deposition is uniformly distributed along the depth. Otherwise for the size ratios in between, the general situation is that the sand deposit decreases with the depth.

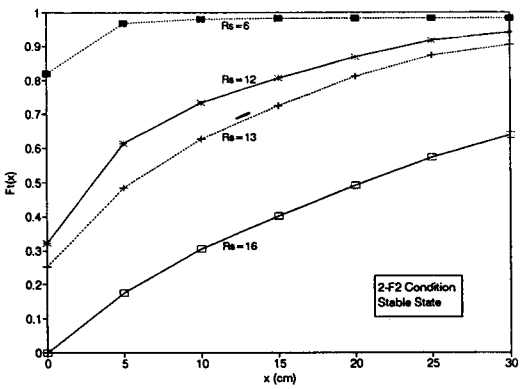

Figure 5. $F_t(x)$ curves for various size ratios at stable state under 2-F2 condition

Variation of $F_t(x)$ with the Total Amount of Sand Input

The amount of sand left on the gravel matrix surface and the amount of sand penetrating through the gravel column are influenced by the total amount of sand introduced into the system. The more the total sand input is, the more the sands left on filter surface and the more the sands passing through the filter are, not only in terms of the absolute amount, but also in terms of the cumulative probability. Figs. 6 and 7 are the $F_t(x)$ curves with various total amounts of sand input under the same conditions at the same running time.

It can be concluded from these experimental results that the efficiency of sand removal by the gravel matrix decreases with the increasing total amount of sand input. However in Fig. 6, there exists a limit line with a very mild slope as the total amount of sand input keeps increasing. This limit line indicates that if an excess amount of sand is introduced into the system, the majority part of the sand would stay on the bed surface to form a thick cake.

For the $F_t(x)$ curves of high R_s in Fig. 7, the gravel matrix acts like a sink and the sand particles are too fine to be trapped within the porous matrix. For example, over 70% (over 11 kg) of the sands penetrate through the gravel column during 20 minutes for the 16 kg sand input while there are only less than 40% (less than 1 kg) of the sands passing through the gravel column during the same period of time for the 2 kg sand input.

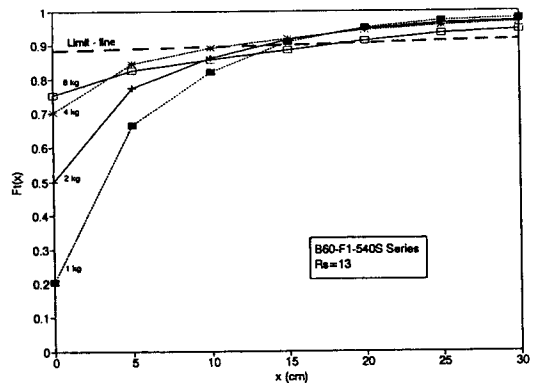

Figure 6. $F_t(x)$ curves of B60-F1-540S series experiments with various total sand inputs

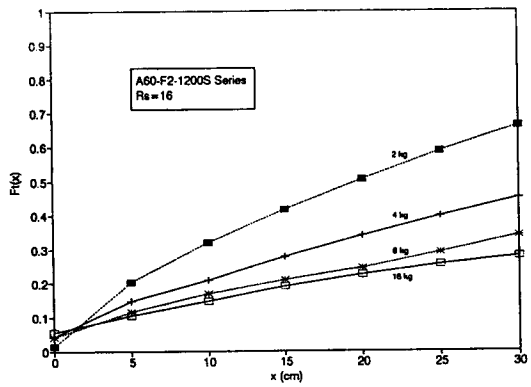

Figure 7. $F_t(x)$ curves of A60-F2-1200S series experiments with various total sand inputs

Variation of $F_t(x)$ with the Seepage Flow Rate

The seepage force induced by the seepage flow does have some influence on the $F_t(x)$ curves as

shown in Fig. 8 even though the actual seepage velocity through the pores is less than 30% the fall velocity based on d_{50} of the #30 sand particles when the seepage flow rate is set to 6 gpm.

The seepage flow with high flow rate carries more sand particles through the filter than the seepage flow with low flow rate under the same conditions. In other words, a lower efficiency of sand removal is achieved by the gravel matrix under the higher seepage flow rate. This can be extended to the case of the granular filter used as the sediment trap for groundwater recharge. During the recharge operation, it is generally desired to maintain a high recharge rate in order to achieve a high operation efficiency. However, the low removal efficiency of the filter accompanied with the high recharge rate should be taken into consideration and carefully handled.

From the patterns of the $F_t(x)$ curves shown in Fig. 8, it is noticed that the $F_t(x)$ curves for various seepage flow rates under the same conditions are, roughly speaking, parallel with each other. In other words, the amount of sand deposit within the corresponding layer of the gravel column for different seepage flow rates is approximately the same, while less amount of sand is left on the surface of the gravel matrix for the higher seepage flow rate.

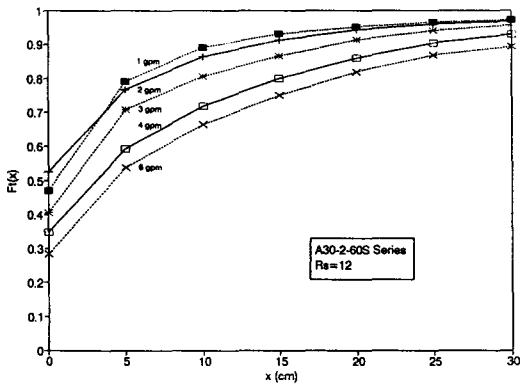

Figure 8. $F_t(x)$ curves of A30-2-60S series experiments with various seepage flow rates

2. The intensity function in time domain, $\lambda_1(t)$

In the preceding paper of this study (Wu, 1994), determination of λ_1 curve by differentiating Λ_1 curve was proposed, where $\Lambda_1(t_i)$ was defined as the integration of $\lambda_1(t)$ from t_0 to t_i, and was given as the following:

$$\Lambda_1(t_i) = -\ln\left[\frac{m_{x_0}(t_i)}{M_T}\right] \tag{2}$$

in which $m_{x_0}(t_i)$ is the amount of sand staying at the bed surface at time t_i. Suppose the experimental data at various times t_0 , t_1 , t_2 , t_3 , ... were available, then the values of $\Lambda_1(t_i)$ at these times can be calculated from Eqn (2). These values of Λ_1 were plotted against the time, and a fitting curve was assigned by a complex regression analysis (Wu, 1993). Total of 7 time series of the experimental data were analyzed by this approach. These 7 best-fit Λ_1 curves are shown in Fig. 9 with the stable Λ_1 value in the parentheses. Once the Λ_1 curves have been obtained, then the λ_1 curves are determined by differentiating the Λ_1 curves. Fig. 10 through Fig. 12 are illustrations of the λ_1 curves so determined. As mentioned in the previous paper (Wu, 1994), the physical interpretation of $\lambda_1(t)$ is the inverse of the average rest period. In other words, large values of $\lambda_1(t)$ imply the short rest periods; and the values of $\lambda_1(t)$ close to zero indicate that the rest periods approach to infinity or the sand particles tend to stay where they are. It is found that the $\lambda_1(t)$ curves are all decreasing with time very fast. When the sand deposit are accumulated within the pore space of the gravel matrix, the size of the pore openings for the sand particles to pass through becomes smaller, as a consequence, the rest period increases with time.

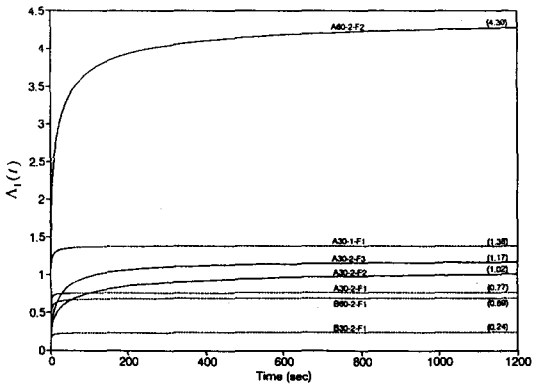

Figure 9. Best-fit $\Lambda_1(t)$ curves for seven series of experiments (with Λ_1^* value in the parentheses)

Variation of $\lambda_1(t)$ with the Size Ratio, R_s

Fig. 10 shows the $\lambda_1(t)$ curves for various size ratios, R_s, under the specified testing condition. From this figure, it is noticed that the magnitude of $\lambda_1(t)$ increases with increasing R_s. This means that the average rest period is longer for lower R_s and the average rest period is shorter for higher R_s. The variation of the rest period with the size ratio may be explained by the following hypothesis. In the case of the clean gravel matrix, the pore openings are relatively larger for the infiltrating sand particles when R_s is higher, consequently the average rest period of the sand particles is shorter. As an analogy, consider two gates of different sizes for the same number of people, say 100, to pass. Five people can pass the larger gate simultaneously whereas only one person can pass the smaller gate at a time. The average time for a person to wait before passing the gate is much shorter for the larger gate, whereas the average waiting time is longer for the smaller gate.

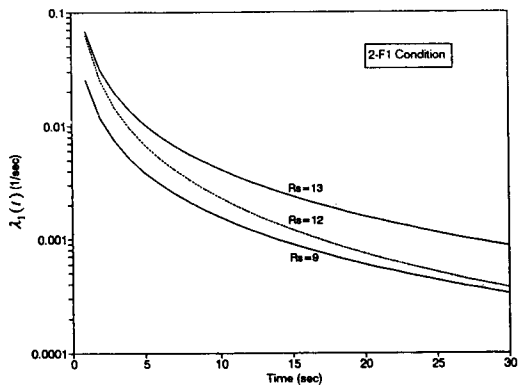

Figure 10. $\lambda_1(t)$ curves for various size ratios under 2-F1 condition

Variation of $\lambda_1(t)$ with the Total Sand Input

Fig. 11 is an illustration of two $\lambda_1(t)$ curves with different total sand input under A30-F1 (type A gravel, #30 sand, and seepage flow at the rate of 1gpm) condition. In Fig. 11, the magnitude of $\lambda_1(t)$ decreases when the total sand input is increasing. In other words, the more the total amount of sand is introduced, the longer the rest period will be. This may be explained by the analogy presented in the previous section. Consider the case of two groups of people, one with 100 people and the other with 20 people, passing through two gates of the same size. If the number of persons allowed to pass the gate at a time is the same, and the moving speed of each person is also the same, then the average time for a person to wait before passing the gate is much longer for the group with 100 people, whereas the average waiting time is shorter for the group with 20 people.

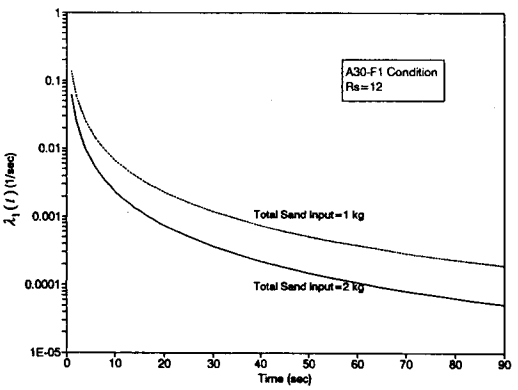

Figure 11. $\lambda_1(t)$ curves for various total sand inputs under A30-F1 condition

Variation of $\lambda_1(t)$ with the Seepage Flow Rate

Fig. 12 is an illustration of three $\lambda_1(t)$ curves subject to different seepage flow rates under A30-2 (type A gravel, and 2 kg of #30 sand) condition. From Fig. 12, it is seen that the magnitude of $\lambda_1(t)$ is smaller for lower seepage flow rate and larger for higher seepage flow rate. The same analogy as previously described is still valid for explaining this phenomenon. Consider two groups of people, with the same number of persons in each group, passing through two gates of the same size, and the number of persons allowed to pass the gate at a time is also the same. The moving speed for each person in one group is faster than that in the other group, then the average time for a person to wait before passing the gate is shorter for the group of people with faster moving speed, whereas the average waiting time is longer for the group of people with slower moving speed.

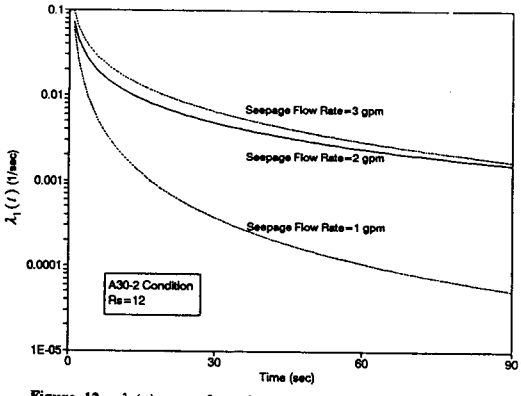

Figure 12. $\lambda_1(t)$ curves for various seepage flow rates under A30-2 condition

3. The intensity function in space domain, $\lambda_2(x)$

The approach for evaluating the intensity function $\lambda_2(x)$ is the first-order finite difference approximation presented in the preceding paper of this study (Wu, 1994), in which the following system of equations is solved for determining $\lambda_2(x)$.

$$\begin{cases} \dfrac{m_{x+\Delta x}(t_i)}{m_x(t_i)} = \exp[-k_2(x)]\cdot\left\{1+k_2(x)\cdot\left[\dfrac{m_{x_0}(t_i)}{m_x(t_i)}+b_i(x)\right]\right\} \\ \dfrac{m_{x-\Delta x}(t_i)}{m_x(t_i)} = \exp[k_2(x)]\cdot\left\{1-k_2(x)\cdot\left[\dfrac{m_{x_0}(t_i)}{m_x(t_i)}+b_i(x)\right]\right\} \end{cases} \tag{3}$$

where $m_{x-\Delta x}(t_i)$ and $m_{x+\Delta x}(t_i)$ are the amounts of sediment that can be found above the depth $x-\Delta x$ and $x+\Delta x$ of the porous matrix at time t_i, respectively. Once $k_2(x)$ and $b_i(x)$ have been solved from Eqn (3) at locations $x = x_1, x_2, \ldots, x_5$, the intensity function $\lambda_2(x)$ at these locations can be calculated:

$$\lambda_2(x) = k_2(x)/\Delta x$$

where the space interval Δx in this study is the thickness of one layer, that is, 5 cm.

The calculated values of λ_2 at locations x_1, x_2, ..., and x_5 were plotted against the depth from the gravel bed surface, and a best-fit curve was assigned by regression analysis. Fig. 13 is an illustration of the calculated λ_2 points and the best-fit curve. The best-fit $\lambda_2(x)$ curve was then substituted back into the cumulative probability distribution function, as given in Eqn (4), to check if the $F_t(x)$ curve calculated from the best-fit $\lambda_2(x)$ curve fits the experimental $F_t(x)$ points.

$$\begin{aligned} F_t(x) &= \exp\left[-\int_{t_0}^{t}\lambda_1(s)ds\right]\cdot\exp\left[-\int_{x_0}^{x}\lambda_2(s)ds\right]\cdot \\ &\quad \sum_{n=0}^{\infty}\sum_{j=n}^{\infty}\frac{\left[\int_{t_0}^{t}\lambda_1(s)ds\right]^n\left[\int_{x_0}^{x}\lambda_2(s)ds\right]^j}{n!\,j!} \\ &= \exp[-\Lambda_1(t)]\exp[-\Lambda_2(x)]\sum_{n=0}^{\infty}\sum_{j=n}^{\infty}\frac{[\Lambda_1(t)]^n[\Lambda_2(x)]^j}{n!\,j!} \end{aligned} \tag{4}$$

Fig. 14 is the comparison of the experimental $F_t(x)$ points with the computed $F_t(x)$ curve. Total of 18 experiments were analyzed by this approach. In summary, it is found that the best-fit $\lambda_2(x)$ curves are generally decreasing exponentially with the depth x:

$$\lambda_2(x) = \lambda_0 \cdot e^{-kx} \tag{5}$$

where λ_0 and k are the coefficients of the best-fit curve. The coefficients λ_0 and k for these 18 experiments are listed in Table 4.

There is one thing to be clarified at this point. It is recalled in the previous paper (Wu, 1994), three infiltration patterns have been introduced:

(I) Surface deposition,
(II) Deep-bed infiltration,
(III) Penetration.

As observed experimentally as well as concluded from the patterns of the experimental $F_t(x)$ curves, the 18 analyzed experiments can be categorized as the following:

(I) Surface deposition:
A1C series (R_s= 6)
B30 series (R_s= 9)
(II) Deep-bed infiltration:
A30 series (R_s= 12)
B60 series (R_s= 13)

(III) Penetration:

A60 series (R_s= 16)

The mechanisms of surface deposition and deep-bed infiltration are similar in terms of the deposition of fine particles within the porous matrix. For these two categories, the fine deposit at any location within the porous matrix increases with time although the fine particles only deposit in the first one or two layers of the porous column for surface deposition, whereas the amount of fines left on top of the porous bed surface decreases with time until the fine deposit within the top layer of the porous column reaches the clogging state. However, the mechanism of penetration is totally different. The amount of fines in each layer increases at the first stage, then remains steady for a while at the second stage. When all the fines on the top of the porous bed surface get into the porous matrix and no additional fines are introduced into the porous matrix system, the amount of fines in each layer decreases at the third stage. Eventually, the major part of the fines penetrates through the porous column and only the minor part is deposited within the porous matrix. For this reason, the $\lambda_2(x)$ curves for A60 series experiments should be treated separately from those of surface deposition and deep-bed infiltration.

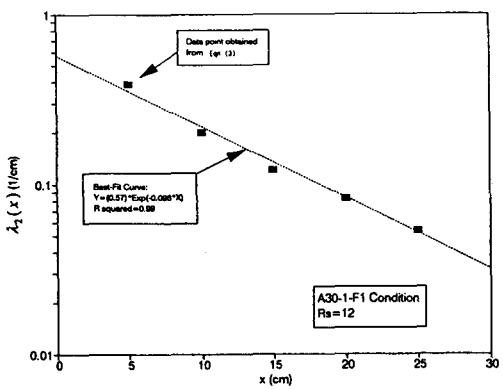

Figure 13. Calculated λ_2 points and the best-fit curve for A30-1-F1 experiment

Variation of $\lambda_2(x)$ with the Size Ratio, R_s

It has been mentioned (Wu, 1994) that the physical interpretation of $\lambda_2(x)$ is the inverse of the average step length. In other words, large values of $\lambda_2(x)$ imply the short average step length whereas the small values of $\lambda_2(x)$ indicate the large average step length of the sand particles.

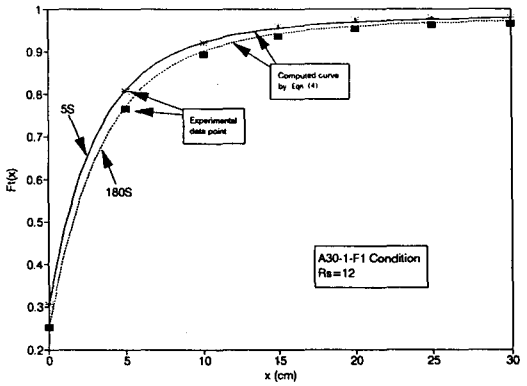

Figure 14. Comparison of the computed $F_t(x)$ curves with the experimental $F_t(x)$ points for A30-1-F1 experiment

TABLE 4 Coefficients of the best-fit $\lambda_2(x)$ curve and category of the infiltration mechanism for the 18 analyzed experiments

Experiment	R_s	λ_0	k	Category
A1C-2-F2	6	0.62	0.240	(I) Surface deposition
A30-1-F1	12	0.57	0.096	(II) Deep-bed infiltration
A30-2-F1	12	0.32	0.073	(II) Deep-bed infiltration
A30-2-F2	12	0.22	0.053	(II) Deep-bed infiltration
A30-2-F4	12	0.19	0.041	(II) Deep-bed infiltration
A30-2-F6	12	0.17	0.035	(II) Deep-bed infiltration
A30-3-F1	12	0.28	0.076	(II) Deep-bed infiltration
A30-4-F2	12	0.14	0.035	(II) Deep-bed infiltration
B30-2-F1	9	0.60	0.185	(I) Surface deposition
B60-1-F1	13	0.43	0.057	(II) Deep-bed infiltration
B60-2-F1	13	0.28	0.065	(II) Deep-bed infiltration
B60-4-F1	13	0.17	0.056	(II) Deep-bed infiltration
B60-8-F1	13	0.08	0.026	(II) Deep-bed infiltration
A60-2-F1	16	0.25	0.043	(III) Penetration
A60-2-F2	16	0.29	0.037	(III) Penetration
A60-4-F2	16	0.12	0.032	(III) Penetration
A60-8-F2	16	0.09	0.030	(III) Penetration
A60-16-F2	16	0.06	0.028	(III) Penetration

Just like $\lambda_1(t)$ is very much dependent on the amount of fine deposit, $\lambda_2(x)$ is also very sensitive to the amount of sand particles deposited within the pore space of the gravel matrix. The following is a possible hypothesis to explain what was observed. Suppose a person is to walk through a room with an entry at one side

of the room and an exit at the opposite side of the room. Consider two different situations: 1) there are 5 persons in the room; and 2) there are 90 persons in the room. The maximum capacity of the room is, say, 100 persons. If the step length is defined by the distance traveled before this person is stopped by any persons in the room since he entered the room. Statistically speaking, the distance traveled before he is stopped in the room with 90 persons would be shorter. This explains why all the $\lambda_2(x)$ curves decreases with the depth. The decreasing trend of $\lambda_2(x)$ curves with the depth means that the average step length is increasing with the depth. This increasing trend of the step length is attributed to the decreasing fine deposit along the depth of the gravel column.

The $\lambda_2(x)$ curves for various size ratios, R_s, under the specified conditions are shown in Figs. 15 and 16. Obviously the pattern of these curves is similar to the pattern of the fine deposition along the depth of the gravel column. For the category of surface deposition (R_s = 6,9), the average step length at the top one or two layers is very small compared to the average step length at deeper layers because of the pattern that the fine deposit is distributed along the depth. In contrast, the average step length is more uniformly distributed along the depth for deep-bed infiltration (R_s = 12,13) and penetration (R_s = 16). It is also noticed that the rate of decay of the $\lambda_2(x)$ curve along the depth decreases with the increasing R_s, except the one in the category of penetration (R_s = 16), as shown in Fig. 16. This is again evidential for the fact that the category of penetration is different from others and should be treated separately.

Variation of $\lambda_2(x)$ with the Total Sand Input

Fig. 17 illustrates the variation of $\lambda_2(x)$ curves with various total sand inputs under the specified testing condition. In this figure, the magnitude of $\lambda_2(x)$ increases with the decreasing total sand input, thus implying that the average step length is larger for larger amount of sand input. Again, the following is the hypothesis to help explaining the observed phenomenon. Consider two groups of people, one with 10 persons and the other with 80 persons, trying to walk through the room as described in the previous section. There are 10 persons standing in the room. As the two groups of people walk through the room, some people are stopped by the persons in the room and some people manage to walk out of the room. Statistically the number of persons that successfully pass the exit is larger for the group with 80 persons, therefore the average distance traveled by this group of people is longer. This is valid for deep-bed infiltration and penetration.

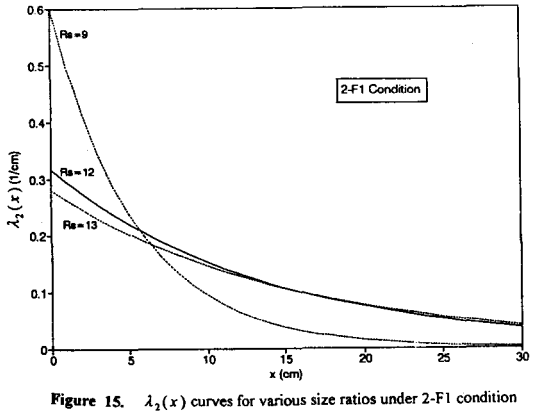

Figure 15. $\lambda_2(x)$ curves for various size ratios under 2-F1 condition

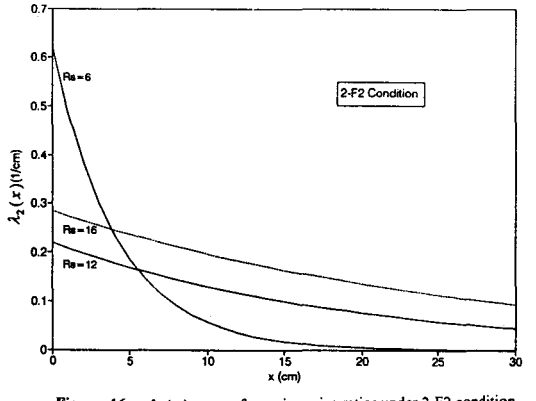

Figure 16. $\lambda_2(x)$ curves for various size ratios under 2-F2 condition

Variation of $\lambda_2(x)$ with the Seepage Flow Rate

Fig. 18 shows four $\lambda_2(x)$ curves subject to various seepage flow rates under the deep-bed infiltration condition. The observed phenomenon is explained as the following. Consider two groups of people, with the same number of persons in each group, are trying to walk through

a room as described previously with different moving speeds. There are several people, say, 10 persons standing in the room. People in the group with faster moving speed are less likely to be stopped and thus the number of persons that pass through the room is larger for the faster group. Therefore the average distance of travel is longer for this group. However, as a consequence of the longer distance of travel, more fine particles deposit into the deeper layers of the gravel column because of the larger amount of sand that comes in. This result is reflected on Fig. 18, which shows the higher magnitude of $\lambda_2(x)$ for higher seepage flow rate and the lower magnitude of $\lambda_2(x)$ for lower seepage flow rate at the deeper layers of the gravel column.

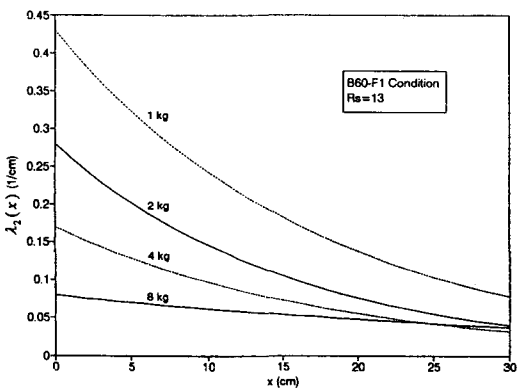

Figure 17. $\lambda_2(x)$ curves for various total sand inputs under B60-F1 condition

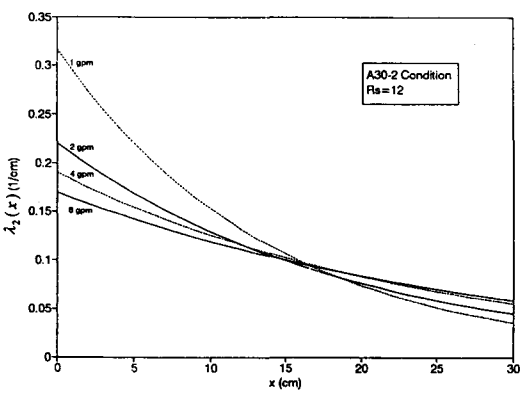

Figure 18. $\lambda_2(x)$ curves for various seepage flow rates under A30-2 condition

APPLICATION

One of the primary objectives of this study is to develop a quantitative model that can serve as a tool in predicting the behavior of the fine particles infiltrating into the porous matrix as well as an aid in designing the filter system. Application of the results obtained from the previous sections is possible only when these results are generalized for the untested or more complex conditions. Since λ_1 and λ_2 are the two parameters of the NHPP model, generalization of λ_1 and λ_2 becomes essential for applying the NHPP model.

Generalization of $\Lambda_1(t)$ at Stable State

When executing the computation of the cumulative probability distribution, $F_i(x)$, given by Eqn (4), it was found that the value of $\Lambda_1(t_i)$ is more useful than the function $\lambda_1(t)$ in calculating the cumulative probability distribution along the depth at the time t_i . Therefore generalization of $\Lambda_1(t)$ is more preferable than generalizing $\lambda_1(t)$. However, it was noticed that generally the process of the sand infiltration into the gravel matrix is so fast that it reaches the stable state or the state close to stable in a very short period of time. The time variation of the amount of sand deposit within the pore space is important for acquiring an insight to the mechanism of infiltration, yet the clogging state is more concerned by the engineers and filter designers.

Fig. 9 illustrates seven best-fit $\Lambda_1(t)$ curves as mentioned previously. It can be seen that $\Lambda_1(t)$ curves climb up very fast in the first 60 seconds, and all of them reach 95% the stable values of $\Lambda_1(t)$ curves within 10 minutes. This rapid change of $\Lambda_1(t)$ curves is attributed to the sudden dumping of a large quantity of sediment on top of the gravel matrix. For this particular experimental condition, regression analysis is performed specifically on the stable values of $\Lambda_1(t)$ curves owing to the following two reasons: 1) the process of sand infiltration into the gravel matrix is such a quick process that it reaches the stable state or the pre-stable state in a short period of time, hence the variation of the sand deposit within this period of time is not a very crucial thing to know; 2) for engineering and filter design purposes, the distribution of sand deposit

along the filter depth at the stable state or the pre-stable state is more important than the variation within a very short period of time.

The stable values of $\Lambda_1(t)$ curves from the seven series of experiments in Fig. 9 are the dependent variables for performing a linear regression analysis, and the independent variables are the size ratio, total sand input, and the non-dimensionalized sand particle velocity. The equation relating the stable value of $\Lambda_1(t)$ curve with the three variables is:

$$\Lambda_1^s = a_1 \cdot R_s^{a_2} \cdot I^{a_3} \cdot V^{a_4} \qquad (6)$$

where

Λ_1^s = the value of $\Lambda_1(t)$ at stable state
$R_s = D_{15}/d_{85}$
I = total sand input in kg
V = sand particle velocity / fall velocity based on d_{50}

$$= \frac{\text{fall velocity + actual seepage velocity through the pores}}{\text{fall velocity based on } d_{50}}$$

$$= \frac{\omega + (Q_s / A_f)/n}{\omega} = 1 + \frac{v_a}{\omega}$$

in which Q_s is the seepage flow rate, A_f is the cross-sectional area of the gravel column, and n is the porosity of the gravel matrix. a_1 through a_4 are the coefficients to be determined by regression analysis.

With the data listed in Table 5, the analysis gives the following result:

$$\Lambda_1^s = (2.42 \times 10^{-5}) \cdot R_s^{4.3} \cdot I^{-1.0} \cdot V^{7.0} \qquad (7)$$

The coefficient of determination, R^2, for the regression is 0.977. The comparison of the regression curve with the data points is shown in Fig. 19. It is found from Fig. 19 that the valid range of application for Eqn (7) is:

$$0.22 \le \Lambda_1^s \le 3.95 \qquad (8)$$

with maximum R_s at 16.34.

TABLE 5. Data used in the regression analysis on Λ_1^s

Series	R_s $(=D_{15}/d_{85})$	I (kg)	V $(=1+v_a/\omega)$	Λ_1^s
A30-1-F1	12.05	1	1.047	1.38
A30-2-F1	12.05	2	1.047	0.77
A30-2-F2	12.05	2	1.094	1.02
A30-2-F3	12.05	2	1.142	1.17
A60-2-F2	16.34	2	1.116	4.30
B30-2-F1	9.29	2	1.047	0.24
B60-2-F1	12.60	2	1.058	0.69

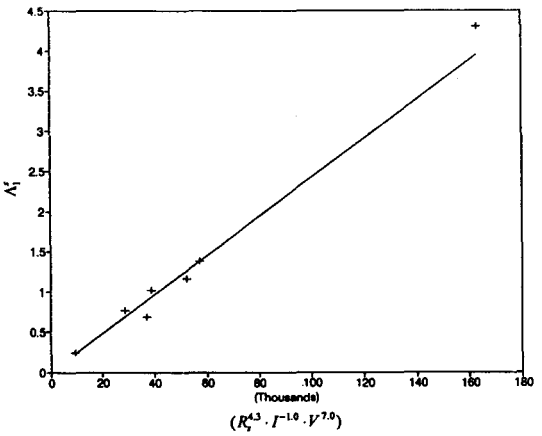

Figure 19. Comparison of the regression curve with data points for Λ_1^s

Generalization of $\lambda_2(x)$ curves

Unlike $\lambda_1(t)$, the intensity function $\lambda_2(x)$ plays a significant role in the computation of $F_t(x)$ because it decides the distribution pattern of the $F_t(x)$ curve. With the value of $\Lambda_1(t_i)$ at the specific time t_i and the intensity function $\lambda_2(x)$, the cumulative probability distribution of the sand deposit along the gravel column at the time t_i can be computed.

As mentioned previously, the general functional form of $\lambda_2(x)$ curves is a natural exponential curve with two parameters λ_0 and k. λ_0 and k are correlated to the three variables described in the previous section. A summary of these relationships is as follows:

$$\begin{cases} \lambda_2(x) = \lambda_0 \cdot e^{-kx} \\ \lambda_0 = a_1 \cdot R_s^{a_2} \cdot I^{a_3} \cdot V^{a_4} \\ k = a_5 \cdot R_s^{a_6} \cdot I^{a_7} \cdot V^{a_8} \end{cases} \qquad (9)$$

in which a_1 through a_8 are the coefficients to be determined by regression analysis.

It has been mentioned that the category of penetration should be treated separately from the categories of surface deposition and deep-bed infiltration. Therefore the regression analysis is performed for two groups of data with different ranks of the gravel-sand size ratio, namely: 1) $6 \le R_s \le 13$; and 2) $R_s = 16$. These two groups of data used in the regression analysis are listed in Tables 6 and 7. The results of the regression analysis are as follows:

1) For $6 \le R_s \le 13$,

$$\begin{cases} \lambda_2(x) = \lambda_0 \cdot e^{-kx} \\ \lambda_0 = (14.33) \cdot R_s^{-1.2} \cdot I^{-0.8} \cdot V^{-3.5} \\ k = (21.36) \cdot R_s^{-2.1} \cdot I^{-0.4} \cdot V^{-3.9} \end{cases} \tag{10}$$

The coefficients of determination, R^2, for λ_0 and k are 0.939 and 0.875 respectively. The regression curves and the data points for λ_0 and k are compared in Figs. 20 and 21. The valid ranges of application for Eqn (10) are:

Table 6 Data used in the regression analysis on $\lambda_2(x)$ for $6 \le R_s \le 13$

Experiment	R_s ($=D_{15}/d_{85}$)	I (kg)	V ($=1+v_a/\omega$)	λ_0	k
A1C-2-F2	6.05	2	1.056	0.62	0.240
A30-1-F1	12.05	1	1.047	0.57	0.096
A30-2-F1	12.05	2	1.047	0.32	0.073
A30-2-F2	12.05	2	1.094	0.22	0.053
A30-2-F4	12.05	2	1.189	0.19	0.041
A30-2-F6	12.05	2	1.283	0.17	0.035
A30-3-F1	12.05	3	1.047	0.28	0.076
A30-4-F2	12.05	4	1.094	0.14	0.035
B30-2-F1	9.29	2	1.047	0.60	0.185
B60-1-F1	12.60	1	1.058	0.43	0.057
B60-2-F1	12.60	2	1.058	0.28	0.065
B60-4-F1	12.60	4	1.058	0.17	0.056
B60-8-F1	12.60	8	1.058	0.08	0.026

Table 7 Data used in the regression analysis on $\lambda_2(x)$ for $R_s = 16$

Experiment	I (kg)	V ($=1+v_a/\omega$)	λ_0	k
A60-2-F1	2	1.058	0.250	0.043
A60-2-F2	2	1.116	0.285	0.037
A60-4-F2	4	1.116	0.120	0.032
A60-8-F2	8	1.116	0.088	0.030
A60-16-F2	16	1.116	0.060	0.028

$$\begin{cases} 0.09 \le \lambda_0 \le 0.72 \\ 0.03 \le k \le 0.29 \end{cases} \tag{11}$$

2) For $R_s = 16$,

$$\begin{cases} \lambda_2(x) = \lambda_0 \cdot e^{-kx} \\ \lambda_0 = (0.42) \cdot I^{-0.7} \cdot V^{-0.4} \\ k = (0.06) \cdot I^{-0.1} \cdot V^{-3.4} \end{cases} \tag{12}$$

The coefficients of determination, R^2, for λ_0 and k are 0.957 and 0.975 respectively. The regression curves and the data points for λ_0 and k are compared in Figs. 22 and 23. The valid ranges of application for Eqn (12) are:

$$\begin{cases} 0.05 \le \lambda_0 \le 0.25 \\ 0.027 \le k \le 0.043 \end{cases} \tag{13}$$

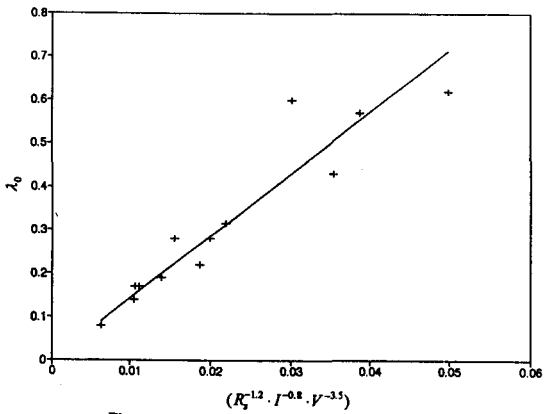

Figure 20. Comparison of the regression curve with data points for λ_0 ($6 \le R_s \le 13$)

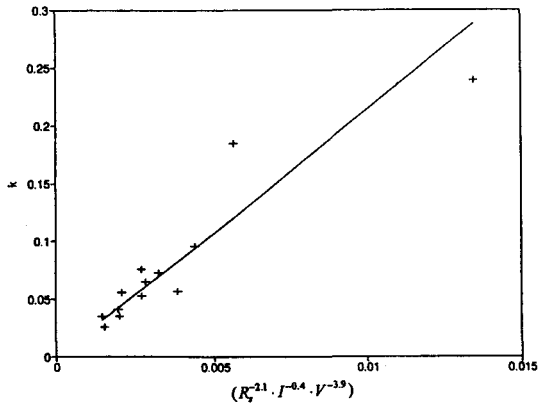

Figure 21. Comparison of the regression curve with data points for k ($6 \le R_s \le 13$)

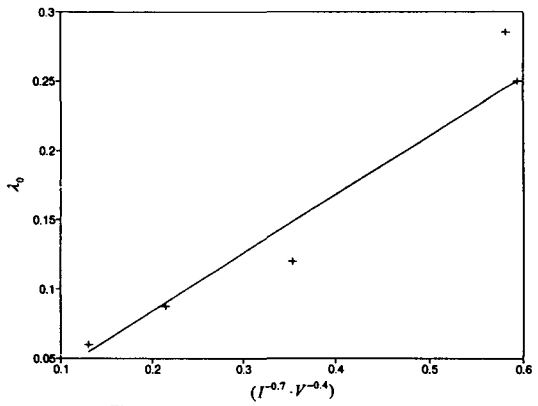

Figure 22. Comparison of the regression curve with data points for λ_0 (R_s = 16)

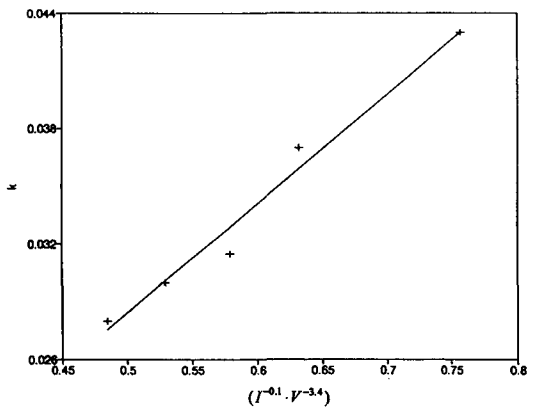

Figure 23. Comparison of the regression curve with data points for k (R_s = 16)

Verification of the Generalized Model

Armed with the two things that have been generalized: 1) the value of $\Lambda_1(t)$ at stable state, Λ_1^s; and 2) the intensity function $\lambda_2(x)$, the NHPP model can be applied to predict the distribution of sand deposition within the gravel column given the corresponding conditions in the valid ranges of application. In the following, two series of experiments are conducted to verify the predicted results.

(1) Experiments with Stratified Gravel Matrix

Three experiments were performed with coarse-to-fine stratified gravel column as shown in Fig. 24. They are:

Gravel column S1:
Experiment S1.60-2-F2-1200S: 4 layers of type A gravel on top of 2 layers of type B gravel,
Gravel column S2:
Experiment S2.60-2-F2-1200S: 3 layers of type A gravel on top of 3 layers of type B gravel,
Gravel column S3:
Experiment S3.60-2-F2-1200S: 2 layers of type A gravel on top of 4 layers of type B gravel.

In each run of these experiments, the total amount of sand input is 2 kg of #60 sand, the seepage flow rate is set to 2 gpm, and the length of the running time is 20 minutes, which is long enough to reach the stable state for these three runs. The calculation of the cumulative probability distribution within the gravel column for these three experiments was performed by Wu (1993).

The plots of the predicted $F_l(x)$ curves and the data points obtained from the experiments with gravel columns S1, S2, and S3 are shown in Figs. 25 through 27. In these figures, the abrupt increases at the depth x= 20 cm, 15 cm, and 10 cm of the predicted curves are attributed to the amount of sand remained out of the type B gravels at the conjunction face. The sands remained out of the type B gravels are not deposited exclusively at the conjunction face, but instead, they are accumulated from the face up into the type A gravels. The smoothened dashed lines in Figs. 25 through 27 are the actual $F_l(x)$ curves due to this upward-accumulation effect.

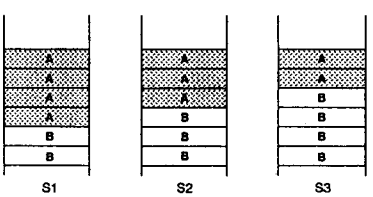

Figure 24. Media distribution in the filter columns S1, S2, and S3

(2) Experiments with Mixed-Size Sand

Three experiments with mixed-size sands infiltrating into the uniformly-graded gravel bed are conducted to verify that the step length is

additive. Consider a sand mixture composed of two kinds of uniform sand, sand A and sand B. The mass composition of the mixture is m_A of sand A and m_B of sand B. If the average step length of the sand A particles at a specific location x is $L_A(x)$ and the average step length of the sand B particles at the same location is $L_B(x)$. Assume that the step length is additive, then the average step length of the mixture at this location is:

$$L_M(x) = \frac{m_A}{m_A + m_B} L_A(x) + \frac{m_B}{m_A + m_B} L_B(x) \qquad (14)$$

where $L_M(x)$ is the average step length of the sand mixture. The physical interpretation of the intensity function $\lambda_2(x)$ is the inverse of the average step length. Therefore Eqn (14) can be rewritten as:

$$\frac{1}{\lambda_2^M(x)} = \frac{m_A}{m_A + m_B} \frac{1}{\lambda_2^A(x)} + \frac{m_B}{m_A + m_B} \frac{1}{\lambda_2^B(x)} \qquad (15)$$

in which $\lambda_2^A(x)$, $\lambda_2^B(x)$, and $\lambda_2^M(x)$ are the intensity functions of sand A, sand B, and the sand mixture respectively. Three experiments carried out for verification are as follows:

Sand mixture M1:

Experiment AM1-2-F1-240S: Mixture of 1.5 kg of #60 sand (75%) and 0.5 kg of #30 sand (25%),

Sand mixture M2:

Experiment AM2-2-F1-240S: Mixture of 1 kg of #60 sand (50%) and 1 kg of #30 sand (50%),

Sand mixture M3:

Experiment AM3-2-F1-240S: Mixture of 0.5 kg of #60 sand (25%) and 1.5 kg of #30 sand (75%).

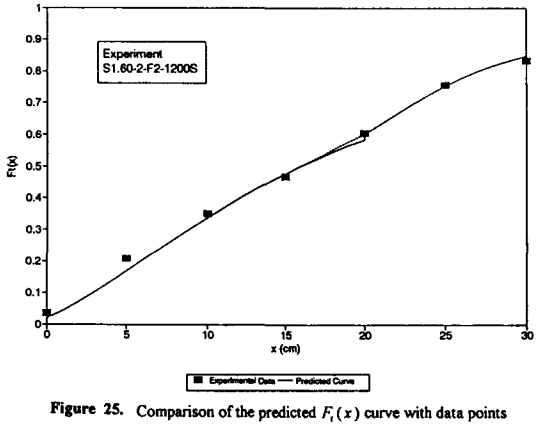

Figure 25. Comparison of the predicted $F_i(x)$ curve with data points for Experiment S1.60-2-F2-1200S

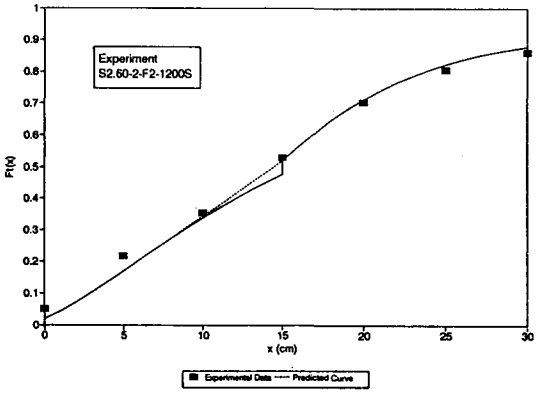

Figure 26. Comparison of the predicted $F_i(x)$ curve with data points for Experiment S2.60-2-F2-1200S

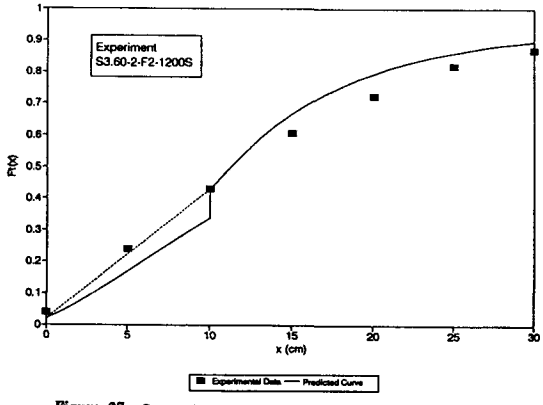

Figure 27. Comparison of the predicted $F_i(x)$ curve with data points for Experiment S3.60-2-F2-1200S

In each run of these three experiments, type A gravel was used to form the porous matrix, the seepage flow rate was set to 1 gpm, and the pre-stable state was reached at 240 seconds.

The $\lambda_2(x)$ curves for mixtures M1, M2, and M3 can be calculated from Eqn (15) since the $\lambda_2(x)$ curves for A30-2-F1 condition and A60-2-F1 condition are given previously. Figure 28 illustrates three $\lambda_2(x)$ curves for conditions AM1-2-F1, AM2-2-F1, AM3-2-F1 as well as two known $\lambda_2(x)$ curves for conditions A60-2-F1 and A30-2-F1. The essential properties of the sand mixtures are listed in Table 8. The plots of the predicted curves with the experimental data points are shown in Fig. 29. The predicted curves for A30-2-F1-240S and A60-2-F1-240S are also shown in Fig. 29. The experimental results for the experiments with stratified gravel beds and the experiments with mixed-size sands are tabulated in Tables 9 and 10.

Table 8. Essential properties of the sand mixtures M1, M2, and M3

Mixture	ω (cm/sec)	d_{50} (mm)	d_{85} (mm)
M1	4.43	0.345	0.472
M2	4.64	0.362	0.503
M3	4.97	0.390	0.536

Table 9. Results of the experiments with stratified gravel matrix

Experiment	m_0 (g)	m_1 (g)	m_2 (g)	m_3 (g)	m_4 (g)	m_5 (g)	m_6 (g)
S1.60-2-F2-1200S	72.43	346.22	282.68	233.92	275.84	303.92	153.59
S2.60-2-F2-1200S	100.93	336.46	269.57	354.06	347.25	205.49	109.49
S3.60-2-F2-1200S	79.53	402.20	381.54	349.85	236.89	189.26	101.95

Table 10. Results of the experiments with mixed-size sand

Experiment	m_0 (g)	m_1 (g)	m_2 (g)	m_3 (g)	m_4 (g)	m_5 (g)	m_6 (g)
AM1-2-F1-240S	438.16	672.48	320.36	176.79	115.67	60.14	38.28
AM2-2-F1-240S	641.45	678.60	290.83	118.66	77.95	35.00	33.67
AM3-2-F1-240S	919.80	591.52	218.40	89.57	57.21	28.86	23.87

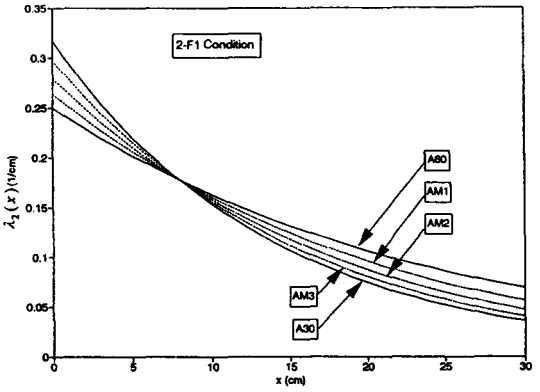

Figure 28. $\lambda_2(x)$ curves for conditions AM1-2-F1, AM2-2-F1, AM3-2-F1, A60-2-F1, and A30-2-F1

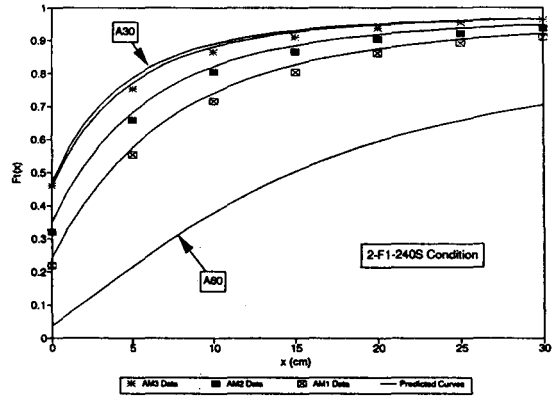

Figure 29. Comparison of the predicted $F_i(x)$ curves with data points for experiments with sand mixtures M1, M2, and M3, and the predicted $F_i(x)$ curves for A30 and A60 conditions

CONCLUSIONS

A non-homogeneous Poisson process (NHPP) model is developed for the physical process of sediment infiltration into the porous media. The approaches for determining the two parameters, λ_1 and λ_2, of the NHPP model are also presented. The results of this study show that sediment infiltration into and deposition within the porous media are described fairly well by this stochastic model. The conclusions made here are valid for the infiltration of instantaneously supplied uniform sediment into the well-sorted gravel column subject to a constant vertical seepage flow.

The model as developed in this study can be applied to describe the physical process associated with the infiltration of fine particles into the coarse porous matrix. Practical examples are sediment deposition into the stream gravel beds, granular filters used as a sediment trap for groundwater recharge, and design of protective filters such as the inverted filter used at the embankment dam site to protect the base soil from piping and the filter blanket underlying the bank protection facility to inhibit the erosion of bank material, among other examples. However, the application of this model to the conditions beyond the scope of this study, such as the infiltration of continuously supplied suspended fines into the broadly-graded gravel matrix subject to the unsteady intergravel flow in the direction other than vertical, still remains to be verified.

REFERENCES

Garde, R. J. and Ranga Raju, K. G., 1985. Mechanics of Sediment Transportation and Alluvial Stream Problems, Wiley Eastern Limited, New Delhi. pp. 23-24.

Sherard, J. L., Dunnigan, L. P. and Talbot, J. R., 1984. Basic Properties of Sand and Gravel Filters. J. Geotech. Eng., ASCE, 110(6): 684-700.

Yim, C. S. and Sternberg, Y. M., 1987. Development and Testing of Granular Filter Design Criteria for Stormwater Management Infiltration Structures

(文轉第27頁)